JGR Space Physics

RESEARCH ARTICLE
10.1029/2020JA028084

Seasonal and Hemispheric Asymmetries of *F* Region Polar Cap Plasma Density: Swarm and CHAMP Observations

S. M. Hatch[1], S. Haaland[1,2], K. M. Laundal[1], T. Moretto[1], A. W. Yau[3], L. Bjoland[1,4], J. P. Reistad[1], A. Ohma[1], and K. Oksavik[1,4]

[1]Birkeland Centre for Space Science, University of Bergen, Bergen, Norway, [2]Max-Planck Institute for Solar Systems Research, Göttingen, Germany, [3]Department of Physics and Astronomy, University of Calgary, Calgary, Alberta, Canada, [4]Department of Arctic Geophysics, University Centre in Svalbard, Longyearbyen, Norway

Key Points:
- Statistics of *F* region polar cap plasma density derived from 15 years of measurements exhibit several types of seasonal asymmetries
- Statistics do not support the conjecture that limited plasma availability is the cause of observed hemispheric asymmetries in lobe density
- Southern Hemisphere polar cap plasma densities lag those in Northern Hemisphere by at least 2 weeks around local spring and fall equinox

Supporting Information:
- Supporting Information S1

Correspondence to:
S. M. Hatch,
Spencer.Hatch@uib.no

Citation:
Hatch, S. M., Haaland, S., Laundal, K. M., Moretto, T., Yau, A., Bjoland, L. M., et al. (2020). Seasonal and hemispheric asymmetries of *F* region polar cap plasma density: Swarm and CHAMP observations. *Journal of Geophysical Research: Space Physics*, *125*, e2020JA028084. https://doi.org/10.1029/2020JA028084

Received 6 APR 2020
Accepted 16 OCT 2020
Accepted article online 31 OCT 2020

Abstract One of the primary mechanisms of loss of Earth's atmosphere is the persistent "cold" ($T \lesssim 20$ eV) ion outflow that has been observed in the magnetospheric lobes over large volumes with dimensions of order several Earth radii. As the main source of this cold ion outflow, the polar cap *F* region ionosphere and conditions within it have a disproportionate influence on these magnetospheric regions. Using 15 years of measurements of plasma density N_e made by the Swarm spacecraft constellation and the Challenging Mini Satellite Payload (CHAMP) spacecraft within the *F* region of the polar cap above 80° Apex magnetic latitude, we report evidence of several types of seasonal asymmetries in polar cap N_e. Among these, the transition between "winter-like" and "summer-like" median polar cap N_e occurs 1 week prior to local spring equinox in the Northern Hemisphere (NH) and 1 week after local spring equinox in the Southern Hemisphere (SH). Thus, the median SH polar cap N_e lags the median NH polar cap N_e by approximately 2 weeks with respect to hemispherically local spring and fall equinox. From interhemispheric comparison of statistical distributions of polar cap plasma density around each equinox and solstice, we find that distributions in the SH are often flatter (i.e., less skewed and kurtotic) than those in the NH. Perhaps of most significance to cold ion outflow, we find no evidence of an *F* region plasma density counterpart to a previously reported hemispheric asymmetry whereby cold plasma density is higher in the NH magnetospheric lobe than in the SH lobe.

Plain Language Summary The Earth's magnetic poles are not perfectly aligned with the Earth's geographic poles, and the degree of misalignment is greater in the Southern Hemisphere. Furthermore, as a result of the Earth's elliptical orbit around the Sun, summer and fall in the Northern Hemisphere together are approximately 1 week longer than summer and fall in the Southern Hemisphere, because the Earth is very slightly closer to the Sun around December solstice (summer in the Southern Hemisphere). These seasonal asymmetries, together with the asymmetric displacement of the Earth's magnetic poles relative to the geographic poles, suggest that the plasma density in the topside ionosphere's geomagnetic polar regions may also be subject to seasonal and hemispheric asymmetries. The polar regions are the primary site of loss of the Earth's atmosphere via so-called ion outflow processes that, over geological time scales, are believed to lead to loss of the Earth's atmosphere. Using 15 years of plasma density measurements made by four different satellites to statistically study the plasma density of each hemisphere's geomagnetic polar cap ionosphere in the altitude range 350–520 km, we find that the polar cap ionosphere at these altitudes exhibits a variety of seasonal and hemispheric asymmetries.

1. Introduction

A substantial fraction of the plasma in the Earth's magnetosphere is supplied by the ionosphere (e.g., Chappell et al., 1987, 2000) through the outflow of ions from the high-latitude polar cap regions, where terrestrial magnetic field lines are open and connected to solar wind magnetic field lines. Ion outflow is the result of ionization of atmospheric gases and outward transport due to vertical forces and is considered to be a primary means of loss of the Earth's atmosphere (e.g., André, 2015). Recent results suggest that low-energy ions from the open polar cap area usually dominate the ion density and the outward flux in populating large volumes of the magnetosphere. Furthermore, ionization (i.e., availability of free charges) rather than transport is thought to be the limiting factor for ion outflow (André et al., 2015; Haaland et al., 2012).

Ionization is primarily driven by solar illumination, although other processes such as cosmic rays (e.g., Adams & Masley, 1965; Velinov, 1970) and particle precipitation also contribute (e.g., Rees, 1963, 1982). Solar radiation at ultraviolet (UV) and extreme ultraviolet (EUV) wavelengths is the most efficient source of ionization in terms of ionizing atmospheric atoms and molecules and producing ion-electron pairs (e.g., Appleton, 1956; Brekke, 1997; Ivanov-Kholodnyy, 1962; Rees, 1989; Schunk & Nagy, 2009). Since the ionosphere as a whole is quasi-neutral, both the electron number density and ion number density are often simply referred to as the plasma density.

The resulting plasma density in the atmosphere is a balance between production (ionization) processes on the one hand and losses by recombination and transport processes on the other hand (e.g., Khocholava, 1977; Quinn & Nisbet, 1965; Rees, 1989; Rishbeth, 1997). Since production and loss processes do not necessarily work on the same time scale, the plasma density at a given location can vary significantly over time. In the terrestrial atmosphere the peak plasma density is typically located in the ionospheric *F* layers, around 200- to 400-km geodetic altitude (e.g., Feldstein et al., 1975; Rishbeth, 1962). Since ionization is strongly driven by solar illumination, plasma density exhibits solar cycle variations as well as strong seasonal and diurnal variations (e.g., Appleton, 1939). Typical plasma densities are of order 10^5–10^6 cm^{-3} in the sunlit ionosphere but can be less by an order of magnitude or 2 in darkness.

In the polar regions the variation of plasma density with season is strongest, followed by diurnal variation and variation with solar cycle (e.g., Feldstein et al., 1975). The seasonal variation can largely be understood on the basis of solar illumination: Under summer conditions, the polar cap is fully illuminated. Conversely, under winter conditions major portions of the polar cap are in complete darkness. The Sun-Earth distance plays a lesser, though nonnegligible, role for variations in solar illumination (e.g., Dang et al., 2017). One would therefore expect solar illumination, ionization, and plasma production around equinox to be very similar in the Northern Hemisphere (NH) and Southern Hemisphere (SH).

In contrast to ionization and production of ionospheric plasma, which are primarily due to solar EUV radiation, transport of ionospheric plasma is driven mostly by electromagnetic forces and is organized with respect to the geomagnetic rather than the geographic poles. Horizontal transport is mainly driven by large-scale magnetospheric convection setup by reconnection at the dayside magnetopause (e.g., Dungey, 1963) and thermospheric neutral winds (e.g., Förster et al., 2008).

Vertical transport—upflow and outflow—is due to a combination of various forces. For example, according to the classical polar wind paradigm (e.g., Axford, 1968; Banks & Holzer, 1968; Dessler & Michel, 1966; Nishida, 1966) light ion species in the ionosphere gain upward mobility via plasma and neutral pressure gradients as well as ambipolar electric fields formed and sustained by requiring charge balance between electrons and ions in the ionosphere. Due to the mirror force, any additional transverse acceleration at the exobase (500–1,000 km) and above effectively acts as upward acceleration (e.g., Klumpar, 1979). At altitudes of a few Earth radii, centrifugal forces (Cladis, 1986; Horwitz et al., 1994; Liu et al., 1994; Nilsson et al., 2008, 2010) become dominant.

Thus, the significant difference in magnetic topology of the NH and SH polar regions (e.g., Cnossen & Förster, 2016; Laundal et al., 2017) is a likely factor in reported hemispheric asymmetries in ionospheric outflow around equinox (e.g., Haaland et al., 2017; Li et al., 2020; Maes et al., 2016). This difference plays a role, for example, in the seasonal variation of thermospheric and ionospheric winds (Aruliah, Farmer, Fuller-Rowell, et al., 1996, Aruliah, Farmer, Rees, & Braändström, 1996; Mikhailov & Schlegel, 2001). Precisely establishing the role of this topological difference in ion outflow is however complicated, since the size and shape of the source regions (primarily the open polar cap and also the cusp and auroral zone) vary greatly in response to solar wind driving (Li et al., 2012; Milan, 2009; Milan et al., 2008; Sotirelis et al., 1998).

In this study, we follow up on previous studies (André et al., 2015; Haaland et al., 2012, 2017) indicating or otherwise suggesting that available ionospheric plasma rather than transport is the limiting factor for cold ion outflow from the polar cap. Using a large database of ionospheric plasma density measurements made by the Swarm and Challenging Mini Satellite Payload (CHAMP) satellites in both hemispheres, we seek to determine under which seasons hemispheric asymmetries in cold plasma outflow might be expected on the basis of available ionospheric plasma.

This study is organized as follows. In section 2 we describe the Swarm and CHAMP combined polar cap plasma density database. In section 3 we identify and describe a number of seasonal and hemispheric asymmetries in polar cap plasma density.

In section 4 we discuss results from the preceding section and describe some implications for cold ion outflow. In section 5 we summarize the results of this study and conclude.

2. Swarm and CHAMP Plasma Density Measurements

We use plasma density measurements made by two separate missions, the original three-satellite Swarm constellation (Friis-Christensen et al., 2008) and the CHAMP satellite (Reigber et al., 2006).

The original three Swarm satellites complete approximately 15 orbits per day in a near-polar orbit, over the 6-year period extending from launch on 22 November 2013 to the present. The two lower satellites, Swarm Alpha (Swarm A) and Swarm Charlie (Swarm C), cover the range of geodetic altitudes between 445 and 500 km (up to 527 km during commissioning phase); Swarm Bravo (Swarm B) covers the range of geodetic altitudes between 510 and 545 km (down to 500 km during commissioning phase). The Electric Field Instrument (EFI) (Knudsen et al., 2017) aboard the three original Swarm satellites includes two dedicated low-gain and high-gain Langmuir Probes (LPs). The two LPs measure plasma density and electron temperature at 2 Hz. The most complete in-flight calibrations and validations of the Swarm LP plasma density and electron temperature measurements, based on comparisons with plasma density measurements measured by other satellites and ground-based instruments, have been performed by Lomidze et al. (2018).

The CHAMP satellite also completed approximately 15 orbits per day in a near-polar orbit over a ∼10-year period extending from 15 July 2000 to 19 September 2010. The nominal range of geodetic altitudes covered by CHAMP extended over ∼300–455 km. The Planar Langmuir Probe (PLP) instrument (Rother et al., 2005) aboard CHAMP made measurements of plasma density at a 15-s cadence. In-flight calibration of the PLP instrument has been performed by McNamara et al. (2007).

In this study we use all Swarm Level 1B LP plasma density measurements downsampled to 15-s cadence, from the period between 10 December 2013 and 5 February 2020 (https://swarm-diss.eo.esa.int/). Downsampling is achieved by selecting every 30th measurement. We also use all CHAMP Level 2 PLP plasma density measurements from the period between 19 February 2002 and 21 December 2009 (https://dataservices.gfz-potsdam.de/portal/?q=CHAMP*) made at ≥350-km geodetic altitude. We impose this altitude restriction on CHAMP density measurements to ensure that all plasma density measurements are made above the altitude at which the $F2$ layer plasma density peak $hmF2$ is located (e.g., Bjoland et al., 2016; Burns et al., 2012; Shim et al., 2011). To Swarm plasma density measurements, we apply the Lomidze et al. (2018) in-flight calibrations (see Appendix A).

Since ion outflow and ionosphere-magnetosphere coupling are organized by the geomagnetic field, we are here concerned with the geomagnetic polar cap, which we define (Table 1) as the region at and above 80° magnetic latitude in the modified apex coordinate system at a reference geodetic altitude of 110 km (i.e., MA_{110} coordinates) (Laundal & Richmond, 2016; Richmond, 1995). In the MA_{110} coordinate system, which is based on the International Geomagnetic Reference Field (IGRF) model (Thébault et al., 2015), all points along a particular IGRF field line have the same magnetic latitude (MLat) and longitude (MLon). To find the MLat and MLon of a satellite at a particular time, the location of the satellite is traced earthward, along the relevant IGRF field line, to the 110-km reference altitude. We perform the conversion of geocentric coordinates to MA_{110} coordinates via the `apexpy` Python package (Emmert et al., 2010; van der Meeren et al., 2018). Table 1 summarizes some properties of the polar caps in each coordinate system.

The total numbers of plasma density (N_e) measurements in the NH and SH geomagnetic polar caps are respectively 2,410,423 and 1,045,654. There are two primary reasons that the statistical coverage of the NH geomagnetic polar cap is greater. First, as a result of the greater displacement of the SH geomagnetic pole relative to the geographic pole than the displacement in the NH, the Swarm and CHAMP satellites pass less frequently through the SH geomagnetic polar cap. Second, the SH geomagnetic polar cap area is approximately 9% smaller than the NH geomagnetic polar cap area (Table 1 and Figure S1 in supporting information). The difference in geomagnetic polar cap area arises because the Earth's magnetic field is stronger in the vicinity of the SH magnetic pole than in the vicinity of the NH magnetic pole (Laundal et al., 2017). The measurement coverage is approximately the same in both hemispheres (2.64 and 2.68 million

Table 1
Definitions and Properties of the Geomagnetic and Geocentric Polar Caps

Hemisphere	Polar cap	Area[a] (km^2)	Circumference[a] (km)
	Geomagnetic (MA_{110}) coordinates		
North	$\geq 80°$ MLat[b]	3.98×10^6	7.11×10^3
South	$\leq -80°$ MLat	3.65×10^6	6.76×10^3
	Geocentric coordinates		
North	$\geq 80°$ Lat[c]	3.91×10^6	6.98×10^3
South	$\leq -80°$ Lat	3.91×10^6	6.98×10^3

[a]Area and perimeter at 0-km altitude. [b]MLat ≡ Magnetic latitude in MA_{110} coordinates (see text). [c]Lat ≡ Latitude in geocentric coordinates.

measurements in the NH and SH geocentric polar caps, respectively) if one instead considers the polar caps defined in a geocentric coordinate system.

In the remainder of the manuscript all references to N_e and statistics refer only to measurements made in the geomagnetic polar caps, unless specified otherwise.

We seek to investigate seasonal and hemispheric asymmetries via statistical comparison of plasma density measurements in the geomagnetic polar cap made by different satellites. Such an investigation is complicated by a number of factors, including the following:

1. Differences in the altitudes of each satellite, which vary on time scales of days and years due to satellite drag and operational maneuvers and which are systematically different in the two hemispheres due to both the shape of each satellite's orbit and the oblateness of the Earth (Text S2 and Figures S2 and S3 of the supporting information). These differences correspond to sampling of different heights in the ionosphere.
2. Variations in solar and geomagnetic activity, which lead to differences in ionospheric conditions.

We partially account for these factors via (i) application of an empirically derived scale height to N_e measurements that "maps" N_e to a common geodetic altitude of 500 km and (ii) application of an empirically derived correction factor that accounts for the variation of N_e measurements with 10.7-cm wavelength solar radio flux (otherwise known as the $F10.7$ index). The latter correction scales N_e to a nominal solar activity (normalized solar radio flux index) of $\langle F10.7 \rangle_{27} = 80$, where $\langle F\ 10.7 \rangle_{27}$ is a rolling average of the preceding 27 days of the $F10.7$ index. Throughout this manuscript, we use the notation N_e^* to refer to these final adjusted densities. More details about the derivation of the relevant scaling factors are located in Appendix A and in the supporting information. This database of adjusted geomagnetic polar cap density measurements (N_e^*) is publicly available (Hatch et al., 2020).

3. Hemispheric and Seasonal N_e^* Variations

Figure 1a shows N_e^* in the NH (blue) and SH (red) geomagnetic polar caps as a function of day of year. The solid blue and dashed red lines, respectively, indicate the median NH and SH N_e^* values within 10-day bins.

One of the apparent differences between the median N_e^* values in the NH and SH geomagnetic polar caps is that N_e^* takes on more extreme values in the SH than in the NH. This difference may be related to the "ionospheric annual asymmetry," which has to do with $NmF2$, the ionospheric $F2$ layer peak plasma density, being about 30% greater globally around December solstice than around June solstice (Rishbeth & Müller-Wodarg, 2006). The ionospheric annual asymmetry and related phenomena are well documented (e.g., Chartier et al., 2019; Dang et al., 2017; Lei et al., 2016; Mendillo et al., 2005; Rishbeth & Müller-Wodarg, 2006; Sai Gowtam & Tulasi Ram, 2017; Torr et al., 1980; Xiong et al., 2018); the asymmetry is the result of a combination of effects related to solar irradiance, atmospheric chemistry, neutral winds, and the global geomagnetic field configuration. The precise role of the global geomagnetic field configuration, in particular, apparently remains to be determined (Dang et al., 2017).

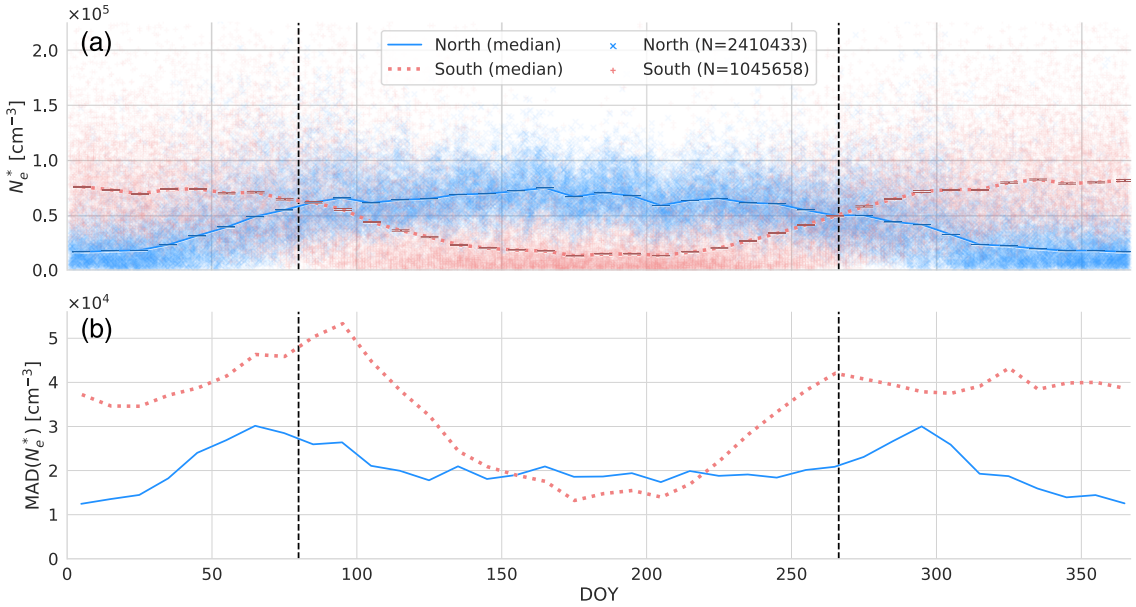

Figure 1. Geomagnetic polar cap plasma density N_e^* statistics versus day of year in the Northern Hemisphere and Southern Hemisphere. Here N_e^* denotes plasma density measurements that are scaled to a common geodetic altitude of 500 km and to a nominal solar activity of $\langle F10.7 \rangle_{27} = 80$, as described in Appendix A. (a) N_e^* measurements and binned medians. The transparent "x" and "+" markers, respectively, indicate 50,000 randomly selected individual measurements made in the NH and SH geomagnetic polar cap for each hemisphere. (Most readers will need to view the plot at full resolution or zoom in to see the distinction between these symbols.) Median N_e^* values within each 10-day bin are, respectively, indicated by the solid blue (north) and dashed red (south) line. Error bars indicate the 95% confidence interval of the bin median, calculated as described in Text S3 of the supporting information. (b) MAD(N_e^*) in the NH (solid blue line) and SH (dashed red line) geomagnetic polar caps, in 10-day bins. In both panels the dotted black lines at DOY ≈ 79.9 and DOY ≈ 266.3, respectively, indicate the average DOY on which March and September equinoxes occur during the years 2000–2020; the time and date of each equinox are calculated as described in section 3. MAD≡median absolute deviation.

Central tendency and variation of a statistical quantity are often indicated by the mean and standard deviation, respectively. However, N_e^* distributions in each bin in Figure 1a are heavy-tailed, and the mean is not a robust indicator of central tendency. In Figure 1a we therefore show median N_e^* statistics in each bin. Likewise, in Figure 1b we show the median absolute deviation

$$\mathrm{MAD}(N_e^*) \equiv \mathrm{median}\left|N_e^* - \mathrm{median}\left(N_e^*\right)\right|$$

instead of standard deviation to indicate the variation of N_e^* in each 10-day bin. Figure 1b shows MAD(N_e^*) in the NH and SH as solid blue and dashed red lines, respectively.

Two salient aspects of MAD(N_e^*) curves in Figure 1b are (i) the SH MAD(N_e^*) is typically greater than NH MAD(N_e^*) and (ii) MAD(N_e^*) in the NH geomagnetic polar cap evinces two distinct peaks, before March equinox and after September equinox, while MAD(N_e^*) in the SH geomagnetic polar cap evinces one primary peak after March equinox, a MAD(N_e^*) "plateau" that extends from September to the end of December and a global minimum near June solstice.

3.1. Asymmetries in Seasonal Variation

We now compare variations in N_e^* as a function of season. We wish to (i) avoid the systematic bias that would be introduced by performing a comparison based on day of year in the Gregorian calendar, which is inherently asymmetric from year to year with respect to the day of year on which equinoxes and solstices occur, and (ii) consistently account for variation in the length of the seasons themselves, which differ on the order of days. To accomplish this, we scale the precise time period between each equinox and solstice for each year such that the period between each equinox and solstice has a duration of 1, and the total duration of all four seasons (i.e., 1 year) is 4. We thus define the "global season parameter" $\phi_s \in [0, 4)$, with March and September equinoxes, respectively, corresponding to $\phi_s = 0$ and $\phi_s = 2$. June and December solstices, respectively, correspond to $\phi_s = 1$ and $\phi_s = 3$. The time stamps of all N_e^* measurements are then scaled to values between 0 and 4. The dates and times of occurrence of each equinox and solstice for all relevant years between 2002 and 2020 are calculated to second precision via the `skyfield` Python package

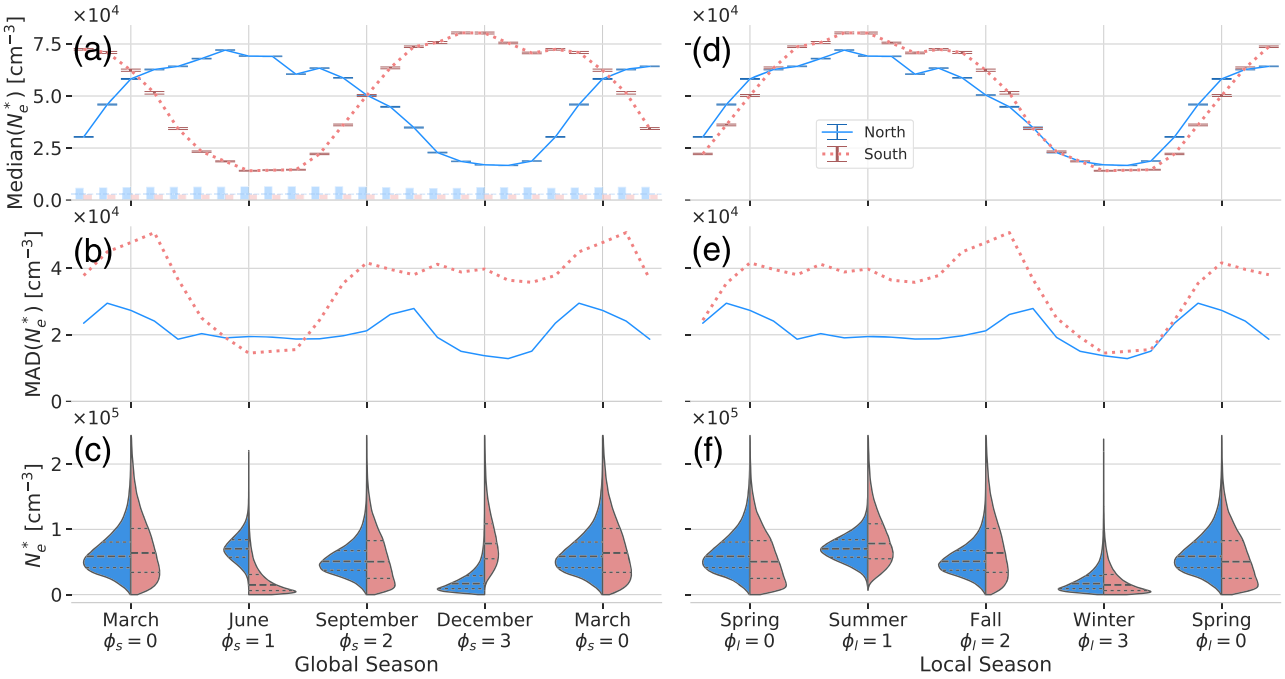

Figure 2. Statistics of Swarm and CHAMP height- and solar flux-adjusted geomagnetic polar cap plasma density N_e^* as a function of global season parameter ϕ_s (left panels; see section 3.1) and local season parameter ϕ_l (right panels) in the Northern Hemisphere (solid blue line) and Southern Hemisphere (dotted red line). The tick marks in each panel precisely indicate the relevant equinox or solstice. Panels (a) and (d) (top row) show median N_e^* in each hemisphere. Each error bar indicates the 95% confidence interval of the median within the corresponding bin, calculated as described in Text S3 of the supporting information. Panels (b) and (e) (middle row) show median absolute deviation (MAD) of N_e^*. Panels (c) and (f) (bottom row) show the distributions of N_e^* in each hemisphere for each season, with statistics taken from ±15 days around the corresponding equinox or solstice. For each distribution, the thick dashed line indicates the median and the two thin dashed lines indicate the first and third quartiles. To facilitate comparison of the transition from December solstice to March equinox (panel c), and from local winter to local spring (panel f), the N_e^* distributions around March equinox and local spring equinox are repeated at far right in each of these panels. The transparent histograms at the bottom of Figure 2a indicate the number of N_e^* values used to calculate the median statistic in each bin. The average number of measurements in each bin is 120,000 in the NH and 52,500 in the SH; the dashed gray line indicates $N = 54{,}000$. The total number of SH measurements is about 60% less than the total number of NH measurements (see section 2).

(Rhodes, 2019). We also define the "local season parameter"

$$\phi_l = \begin{cases} \phi_s & ;\text{NH;} \\ (\phi_s + 2)\ mod 4 & ;\text{SH} \end{cases} \quad (1)$$

to compare N_e^* for the same local season in each hemisphere. For example $\phi_l = 0$, or local spring equinox, corresponds to March equinox in the NH and September equinox in the SH.

Figure 2a displays median N_e^* values in the NH (solid blue line) and SH (dotted red line) geomagnetic polar caps as a function of ϕ_s for bins of 0.2. At March equinox the median value of SH N_e^* is $7 \pm 1\%$ greater than the value of NH N_e^*, while there is apparently no such asymmetry ($0.4 \pm 1\%$) around September equinox.

Figure 2b displays MAD(N_e^*) in each hemisphere as a function of ϕ_s. In addition to the general trends in MAD(N_e^*) described at the beginning of this section, here it is also apparent that the combined hemispheric MAD(N_e^*) at December solstice are greater than the combined hemispheric MAD(N_e^*) around June solstice. The globally greater variability of F region N_e^* around December solstice has been shown (Chartier et al., 2019) to result from a combination of the ionospheric annual asymmetry and O^+ plasma lifetimes that are longer during December solstice than during June solstice.

Figure 2c displays distributions of N_e^* in each hemisphere for March and September equinoxes and for June and December solstice. These distributions represent all N_e^* measurements within ±15 days around the relevant equinox or solstice and indicate multiple aspects of polar cap N_e^* that are not represented by either median or MAD statistics. We discuss these differences in terms of the two other common measures of central tendency, the mean and mode, and in terms of standard deviation. Estimation of the mode of N_e^*, which is a continuous variable, is nontrivial. We estimate the mode via the procedure described by

Table 2
Northern and Southern Hemisphere N_e^* Statistics During Each Equinox and Solstice

Season	Mode	Median	Mean	Std. dev	Skew	Kurtosis
Mar NH	4.95	5.86	6.35	3.10	0.987	1.74
Mar SH	3.59	6.43	7.37	5.10	1.11	1.71
Jun NH	6.70	7.02	7.13	2.03	0.327	0.301
Jun SH	0.31	1.49	2.23	2.26	2.00	5.77
Sep NH	4.66	5.10	5.42	2.40	0.888	1.55
Sep SH	1.49	5.06	5.80	4.16	1.24	4.05
Dec NH	0.83	1.69	2.20	1.89	2.35	9.99
Dec SH	6.26	7.85	8.63	4.29	1.24	2.74
Spring NH	4.95	5.86	6.35	3.10	0.987	1.74
Spring SH	1.49	5.06	5.80	4.16	1.24	4.05
Summer NH	6.70	7.02	7.13	2.03	0.327	0.301
Summer SH	6.26	7.85	8.63	4.29	1.24	2.74
Fall NH	4.66	5.10	5.42	2.40	0.888	1.55
Fall SH	3.59	6.43	7.37	5.10	1.11	1.71
Winter NH	0.83	1.69	2.20	1.89	2.35	9.99
Winter SH	0.31	1.49	2.23	2.26	2.00	5.77

Note. Statistics in columns 2–5 are given in 10^4 cm^{-3}. Statistics in columns 6–7 are unitless.

Bickel and Frühwirth (2006); this methodology yields mode estimates that are very similar (typically differing by less than 0.1%) to mode estimates obtained by identifying the peak of the N_e^* distributions that are shown in Figure 2c.

Table 2 shows that the SH N_e^* distribution mode is greater than the NH N_e^* distribution mode only during December solstice, which is local summer in the SH. On the other hand the SH N_e^* mean is greater than the NH N_e^* mean for all seasons except June solstice, and the SH N_e^* standard deviation is always greater than the NH N_e^* standard deviation. The NH and SH N_e^* distributions otherwise appear most similar during March and September equinox (respectively, $\phi_s = 0$ and $\phi_s = 2$) and most disparate during June and December solstice (respectively, $\phi_s = 1$ and $\phi_s = 3$), as expected. We further discuss the relevance of these differences to cold ion outflow in section 4.

Figure 2d displays median N_e^* values in the NH (solid blue line) and SH (dotted red line) geomagnetic polar caps as a function of ϕ_l. From this figure it is immediately apparent that (i) the range of median SH N_e^* values in the SH is overall larger than the range of median NH N_e^* values, which is also visible in Figure 1a, and (ii) variation in median SH N_e^* lags behind median NH N_e^* around local spring and fall equinoxes by several days. We quantify this lag in the following subsection. These statistics also suggest that the annual maximum in median NH N_e^* occurs before local summer solstice, while the annual maximum in median SH N_e^* occurs at or perhaps slightly before local summer solstice. A secondary peak in median N_e^* between local summer solstice and local fall equinox is also apparent in both hemispheres.

Figure 2e displays MAD(N_e^*) in each hemisphere as a function of ϕ_l. The most immediate observation is that SH MAD(N_e^*) (dotted red line) are almost always greater than NH MAD(N_e^*) (solid blue line), except for the period between local winter and local spring where the MAD(N_e^*) values in each hemisphere are similar. Beyond this basic difference, in both hemispheres MAD(N_e^*) peaks after local fall, reaches a global minimum near local winter, and either peaks (in the NH) or plateaus (in the SH) near local spring.

Figure 2f shows N_e^* distributions in each hemisphere organized by local season. Table 2 indicates that the SH N_e^* distribution mode is always less than the NH N_e^* distribution mode, and the SH N_e^* standard deviation is always greater than the NH N_e^* standard deviation. On the other hand the SH N_e^* mean is less than the NH N_e^* mean only during local spring solstice. The NH and SH N_e^* distributions otherwise appear most similar during local winter solstice ($\phi_l = 3$).

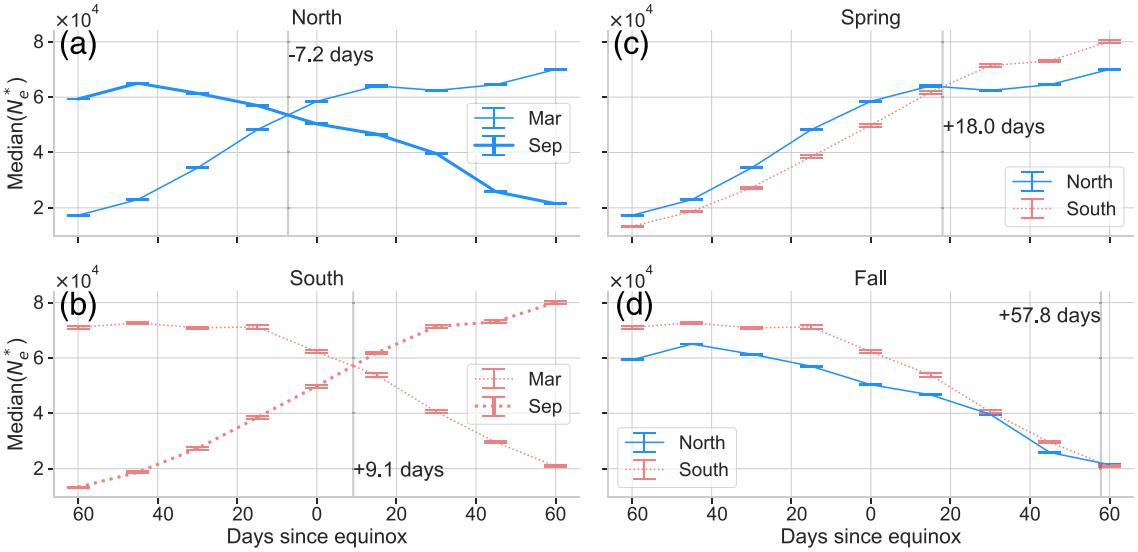

Figure 3. Median N_e^* statistics in 15-day bins relative to the number of days since equinox (Figures 3a–3d). (a) Median NH N_e^* relative to March equinox (thin blue line) and September equinox (thick blue line). (b) Median SH N_e^* relative to March equinox (thin dotted red line) and September equinox (thick dotted red line). (c) Median NH N_e^* (solid blue line) and SH N_e^* (dotted red line) relative to local spring equinox. (d) Median NH N_e^* (solid blue line) and SH N_e^* (dotted red line) relative to local fall equinox. The 95% confidence intervals of the medians in Figures 3a–3d are calculated as described in Text S3 of the supporting information.

3.2. Equinoctial Asymmetries

We now consider the evolution of the median N_e^* in each hemisphere around equinox. Figure 3a shows median NH N_e^* values relative to March equinox (thin blue line) and September equinox (thick blue line) in 15-day bins. Crossover occurs at −7.2 days relative to equinox. Figure 3b shows median SH N_e^* values relative to March equinox (thin red dotted line) and September equinox (thick dotted red line). Crossover occurs at +9.1 days relative to equinox. Figure 3c shows NH and SH median N_e^* values relative to March and September equinox, respectively, and Figure 3d shows NH and SH median N_e^* values relative to September and March equinox, respectively. That is, Figures 3c and 3d show median N_e^* values in each hemisphere relative to local spring and fall, respectively.

Figure 3c shows that the local spring crossover between median NH N_e^* (solid blue line) and median SH N_e^* (dotted red line) occurs at +18 days relative to equinox. Figure 3d shows that the local fall crossover between median NH N_e^* (solid blue line) and median SH N_e^* (dotted red line) occurs at +58 days relative to equinox. However, it should be noted that these two lines also nearly cross at approximately +30 days. To calculate

Table 3
Equinoctial Asymmetries in Median Adjusted Geomagnetic Polar Cap Plasma Density N_e^* Identified in This Study

Asymmetry	Fig	Δt (all sat.) days	Δt (individ. sat.)[a] days
NH/SH Mar crossover delay	1a	4.0	[2.3, 0.4, 10.0, 6.0]
NH/SH Sep crossover[b]	1a	0.4	[1.0, −0.4, 0.4, −2.3]
NH spring/fall crossing	3a	−7.2	[−9.7, −7.6, −6.0, −7.3]
SH spring/fall crossing	3b	9.1	[8.3, 6.5, 14.2, 8.4]
NH/SH spring crossing	3c	18.0	[19.1, 16.7, 19.3, 17.4]
NH/SH fall crossing	3d	57.8[c]	[26.2, 57.8, 60.0, 58.7]

[a]CHAMP, Swarm A, Swarm B, and Swarm C. [b]Evidence for this asymmetry is weak, as Δt is small and exhibits spread around zero. [c]As indicated in section 3.2, median N_e^* in the NH and SH are within a few percent of each other over days 30 to 60 after equinox.

the crossover point in each panel, we interpolate between each 15-day median with a resolution of 0.1 days and determine the relative day of year for which the two lines shown in each panel are nearest each other.

4. Discussion

Results in the preceding section indicate the existence of several seasonal and hemispheric asymmetries in the plasma density of the geomagnetic polar caps. Table 3 summarizes the equinoctial asymmetries identified from Figures 1–3 on the basis of the combined database of Swarm and CHAMP measurements.

A central purpose of this study is to determine whether the hemispheric asymmetry in magnetospheric lobe cold plasma density reported by Haaland et al. (2017) could be explained on the basis of plasma densities in the ionospheric polar caps. In specific, they found that cold plasma densities in the NH lobe were overall greater than the cold plasma densities in the SH lobe around September equinox and speculated whether this asymmetry was due to differences in outflow and plasma densities between NH and SH. No such corresponding asymmetry in median geomagnetic polar cap N_e^* at September equinox is apparent in Figures 1a and 2a. And while there are clear differences between the distributions of N_e^* in each hemisphere at September equinox ($\phi_s = 2$ in Figure 2c), as we discuss in section 3.1, we find no evidence suggesting that NH N_e^* is systematically greater than SH N_e^* around September equinox.

In summary, on the basis of the Swarm and CHAMP N_e^* distributions that we have presented, the hemispheric asymmetry in Cluster-observed cold plasma densities in the magnetospheric lobes (Haaland et al., 2017) has no clear correspondence with plasma densities in the geomagnetic polar caps. We believe that this is the most significant result of this study.

Among the possible causes of the hemispheric asymmetry in lobe cold plasma density are hemispherically asymmetric vertical transport, flux tube volume, or conductivities in the geomagnetic polar caps. Li et al. (2020) have shown, for instance, that the strength of the Earth's magnetic field is anticorrelated with ionospheric outflow. The cause of this apparent discrepancy between Swarm, CHAMP, and Cluster observations will be the subject of future work.

Another significant result of analysis in section 3.2 is displayed in Figure 3. In Figure 3a the crossover point of the two NH (solid blue) lines occurs approximately 7 days before equinox, whereas in Figure 3b the crossover point of the two SH (dotted red) lines occurs approximately 9.1 days after equinox. Thus, the days on which the local hemisphere geomagnetic polar cap density N_e^* crossover near local equinox occurs are hemispherically asymmetric. This asymmetry is also present when the polar caps are defined in geocentric coordinates (not shown) and so is not the result of a particular choice of coordinate system.

Comparison of median N_e^* curves from each geomagnetic polar cap around local spring (Figure 3c) and around local fall (Figure 3d) shows that the crossover points in both hemispheres occur more than 2 weeks after equinox. This suggests the existence of a seasonal "phase offset" between the two hemispheres in median N_e^* around local spring and fall equinoxes, whereby median N_e^* in the SH geomagnetic polar cap lags median N_e^* in the NH geomagnetic polar cap by at least 2 weeks. The lag around local spring equinox is even more pronounced, 6 weeks or more, when the polar caps are defined in geocentric coordinates (not shown).

Thus, the relative lag between SH and NH polar cap N_e^* around local spring equinox is not the result of choosing a particular definition of the polar caps (i.e., geomagnetic versus geocentric; see Table 3). On the other hand there is apparently no lag between SH and NH geocentric polar cap median N_e^* around local fall equinox, which suggests that the relative lag exhibited by median N_e^* in the geomagnetic polar caps is related to the choice of coordinate system (i.e., geomagnetic instead of geocentric polar caps).

The different lags imply that there are at least two contributing factors to the delay, which likely operate somewhat differently in the two sets of polar caps during local spring and local fall. Here it is worth noting that the existence of a relative lag in geomagnetic polar cap N_e^* around local fall equinox may be related to reported hemispheric asymmetry in ion outflow processes and ionosphere-magnetosphere coupling that is organized by the geomagnetic field (André et al., 2015; Haaland et al., 2012, 2017).

To test the robustness of the asymmetries identified in Figures 1–3 and Table 1, we have also performed the analysis separately for each of the four satellites used in this study (not shown). The values obtained from each of these separate analyses are shown in the rightmost column of Table 3. All of the asymmetries we have just discussed also appear in the analyses based on measurements from individual satellites. More

specifically with the exception of the weak evidence for a NH/SH crossover delay at September equinox, the other delays are consistent between all four spacecraft albeit with slight differences in the estimated Δt values.

We believe that these separate analyses are important indicators of the robustness of each asymmetry, since the Swarm and CHAMP satellites monitor polar cap plasma density at effectively three different altitude ranges over two different portions of a solar cycle, with two different and independent types of LP instruments and three different orbits.

5. Summary

Using 15 years of plasma density measurements made by the original three Swarm satellites and the CHAMP satellite, we have identified equinoctial asymmetries in *F* region ionospheric plasma density in the geomagnetic polar caps. In particular:

1. Haaland et al. (2017) have reported overall lower cold plasma densities in the SH magnetospheric lobe relative to the NH magnetospheric lobe around September equinox; they conjecture that the difference may be related to available ionospheric plasma in the polar cap. We find no evidence supporting this conjecture.
2. We present evidence that SH polar cap plasma density lags behind NH polar cap plasma density by at least 2 weeks around March and September equinox.
3. For every season the SH distribution of *F* region polar cap plasma density is spread over a wider range of values than the NH distribution. The mode of the SH distribution is also generally lower than the mode of the NH distribution.

Appendix A: Correction and Adjustment of Ne

Here we provide some additional details on the procedure for obtaining the final height- and solar flux-adjusted density measurements that are denoted N_e^* throughout the manuscript. A detailed description of this procedure and relevant figures is located in Text S2 and Figures S2 and S3 of the supporting information.

After applying the Lomidze et al. (2018) in-flight calibrations to Swarm plasma density measurements, we additionally account for differences in altitude and solar activity via (i) application of an empirically derived scale height to N_e measurements that "maps" N_e to a common geodetic altitude of 500 km and (ii) application of an empirically derived correction factor that accounts for the variation of N_e measurements with 10.7-cm solar radio flux (otherwise known as the $F10.7$ index).

As pointed out in section 2 the CHAMP satellite and the three Swarm satellites cover different altitude ranges and thus different portions of the *F* region. The altitude range covered by the CHAMP satellite (315–455 km) is the lowest of all four satellites, while the altitude range covered by Swarm B (500–545 km) is mostly above those of the other satellites.

From 380 conjunctions between Swarm B and either Swarm A or Swarm C for which Swarm LP data are currently available (December 2013 through February 2020), we derive the Vertical Scale Height VSH $\equiv dh/(d\ln N_e)$ (e.g., Hu et al., 2019). We use "robust regression" (e.g., Holland & Welsch, 1977; Huber, 1973) to estimate VSH from the ratio of plasma density measurements during the 380 identified conjunctions (Figure S2c in supporting information). From this regression we obtain VSH values of 205 km on the dayside ($6 \le \mathrm{MLT} < 18$) and 167 km on the nightside ($\mathrm{MLT} < 6$ and $\mathrm{MLT} \ge 18$). These scale heights are within the range of typical estimates at geodetic altitudes of 350–500 km (e.g., Figure 2 in Hu et al., 2019 and Figure 1b in Stankov & Jakowski, 2006).

To each N_e measurement, we then apply a scaling factor

$$N_{e,h_0} = N_e \exp\left[\left(h - h_0\right)/\mathrm{VSH}\right], \tag{A1}$$

where h is the altitude at which the measurement is made. We arbitrarily select a reference geodetic altitude $h_0 = 500$ km. This scaling decreases the value of N_e for measurements made below h_0 and increases the value of N_e for measurements made above h_0.

In addition to variation with altitude polar cap N_e also varies approximately linearly with $\langle F\ 10.7\rangle_{27}$, an average of the $F10.7$ index during the preceding 27 days. We use $\langle F\ 10.7\rangle_{27}$, as a proxy for solar EUV intensity. Another common choice for averaging the $F10.7$ index is a centered 81-day window (e.g., Liu & Chen, 2009; Schunk & Nagy, 2009). We have elected to use $\langle F\ 10.7\rangle_{27}$ instead, since we find that the RMS error between this quantity and N_{e,h_0} is slightly (~5%) lower than the RMS error between an 81-day centered average of the $F10.7$ index and N_{e,h_0}.

We use robust regression to fit N_{e,h_0} and $\langle F\ 10.7\rangle_{27}$ values with a model of the form

$$N_{e,h_0} = A\langle F10.7\rangle_{27} - B = N\left(a\langle F10.7\rangle_{27} - 1\right). \tag{A2}$$

The resulting best fit model parameters are $a = 0.02564$ and $N = 46{,}780\ \mathrm{cm}^{-3}$. We apply the portion of the model in Equation A2 that is dependent on $\langle F\ 10.7\rangle_{27}$, namely, the parameter a, to each N_{e,h_0} value to finally obtain the height- and solar flux-adjusted density

$$N_e^* = N_{e,h_0}\frac{80a - 1}{a\langle F10.7\rangle_{27} - 1}. \tag{A3}$$

The numerator in Equation A3 scales the final adjusted density N_e to a nominal solar flux level of $\langle F10.7\rangle_{27} = 80$. (Final adjusted densities are shown in Figure S3b of the supporting information.)

Data Availability Statement

The Level 2 CHAMP PLP data set and Level 1B Swarm LP data set are publicly accessible via https://dataservices.gfz-potsdam.de/portal/?q=CHAMP* and https://swarm-diss.eo.esa.int/, respectively. The $F10.7$ index is available via the NASA OMNI database (https://omniweb.gsfc.nasa.gov/form/dx1.html). The database of adjusted geomagnetic polar cap density measurements, denoted N_e^* in the manuscript, is also publicly available (Hatch et al., 2020) (https://doi.org/10.5281/zenodo.3813145).

Acknowledgments
Work at the Birkeland Center for Space Science and the University of Bergen was funded by the Research Council of Norway/CoE under Contract 223252/F50 and by ESA Contract 4000126731 in the framework of EO Science for Society.

References

Adams, G. W., & Masley, A. J. (1965). Production rates and electron densities in the lower ionosphere due to solar cosmic rays. *Journal of Atmospheric and Terrestrial Physics*, *27*(3), 289–298. https://doi.org/10.1016/0021-9169(65)90029-2

André, M. (2015). Previously hidden low-energy ions: A better map of near-Earth space and the terrestrial mass balance. *Physica Scripta*, *90*(12), 128005. https://doi.org/10.1088/0031-8949/90/12/128005

André, M., Li, K., & Eriksson, A. I. (2015). Outflow of low-energy ions and the solar cycle. *Journal of Geophysical Research: Space Physics*, *120*, 1072–1085. https://doi.org/10.1002/2014JA020714

Appleton, E. V. (1939). Characteristic variation of region f_2 ionization throughout the year. *Nature*, *144*(3638), 151–152. https://doi.org/10.1038/144151a0

Appleton, E. V. (1956). Regularities and irregularities in the ionosphere. *Vistas in Astronomy*, *2*(1), 779–790. https://doi.org/10.1016/0083-6656(56)90001-0

Aruliah, A. L., Farmer, A. D., Fuller-Rowell, T. J., Wild, M. N., Hapgood, M., & Rees, D. (1996). An equinoctial asymmetry in the high-latitude thermosphere and ionosphere. *Journal of Geophysical Research*, *101*, 15,713–15,722. https://doi.org/10.1029/95JA01102

Aruliah, A. L., Farmer, A. D., Rees, D., & Brändström, U. (1996). The seasonal behavior of high-latitude thermospheric winds and ion velocities observed over one solar cycle. *Journal of Geophysical Research*, *101*, 15,701–15,712. https://doi.org/10.1029/96JA00360

Axford, W. I. (1968). The polar wind and the terrestrial helium budget. *Journal of Geophysical Research*, *73*, 6855–6859. https://doi.org/10.1029/JA073i021p06855

Banks, P. M., & Holzer, T. E. (1968). The polar wind. *Journal of Geophysical Research*, *73*(21), 6846–6854. https://doi.org/10.1029/JA073i021p06846

Bickel, D. R., & Frühwirth, R. (2006). On a fast, robust estimator of the mode: Comparisons to other robust estimators with applications. *Computational Statistics & Data Analysis*, *50*(12), 3500–3530. https://doi.org/10.1016/j.csda.2005.07.011

Bjoland, L. M., Belyey, V., Løvhaug, U. P., & La Hoz, C. (2016). An evaluation of international reference ionosphere electron density in the polar cap and cusp using EISCAT Svalbard radar measurements. *Annales Geophysicae*, *34*(9), 751–758. https://doi.org/10.5194/angeo-34-751-2016

Brekke, A. (1997). *Physics of the polar upper atmosphere*. Springer Nature.

Burns, A. G., Solomon, S. C., Wang, W., Qian, L., Zhang, Y., & Paxton, L. J. (2012). Daytime climatology of ionospheric NmF2 and hmF2 from COSMIC data. *Journal of Geophysical Research*, *117*, A09315. https://doi.org/10.1029/2012JA017529

Chappell, C. R., Giles, B. L., Moore, T. E., Delcourt, D. C., Craven, P. D., & Chandler, M. O. (2000). The adequacy of the ionospheric source in supplying magnetospheric plasma. *Journal of Atmospheric and Solar-Terrestrial Physics*, *62*, 421–436. https://doi.org/10.1016/S1364-6826(00)00021-3

Chappell, C. R., Moore, T. E., & Waite, J. H. (1987). The ionosphere as a fully adequate source of plasma for the Earth's magnetosphere. *Journal of Geophysical Research*, *92*, 5896–5910. https://doi.org/10.1029/JA092iA06p05896

Chartier, A. T., Huba, J. D., & Mitchell, C. N. (2019). On the annual asymmetry of high latitude sporadic F. *Space Weather*, *17*, 1618–1626. https://doi.org/10.1029/2019SW002305

Cladis, J. B. (1986). Parallel acceleration and transport of ions from polar ionosphere to plasma sheet. *Geophysical Research Letters*, *13*, 893–896. https://doi.org/10.1029/GL013i009p00893

Cnossen, I., & Förster, M. (2016). North-south asymmetries in the polar thermosphere-ionosphere system: Solar cycle and seasonal influences. *Journal of Geophysical Research: Space Physics*, *121*, 612–627. https://doi.org/10.1002/2015JA021750
Conover, W. J. (1999). *Practical nonparametric statistics* (3rd ed.). John Wiley & Sons.
Dang, T., Wang, W., Burns, A., Dou, X., Wan, W., & Lei, J. (2017). Simulations of the ionospheric annual asymmetry: Sun-Earth distance effect. *Journal of Geophysical Research: Space Physics*, *122*, 6727–6736. https://doi.org/10.1002/2017JA024188
Dessler, A. J., & Michel, F. C. (1966). Plasma in the geomagnetic tail. *Journal of Geophysical Research*, *71*(5), 1421–1426. https://doi.org/10.1029/JZ071i005p01421
Dungey, J. W. (1963). Interactions of solar plasma with the geomagnetic field. *Planetary and Space Science*, *10*, 233–237. https://doi.org/10.1016/0032-0633(63)90020-5
Emmert, J. T., Richmond, A. D., & Drob, D. P. (2010). A computationally compact representation of magnetic-apex and Quasi-dipole coordinates with smooth base vectors. *Journal of Geophysical Research*, *115*, A08322. https://doi.org/10.1029/2010JA015326
Förster, M., Rentz, S., Köhler, W., Liu, H., & Haaland, S. E. (2008). IMF dependence of high-latitude thermospheric wind pattern derived from CHAMP cross-track measurements. *Annales Geophysicae*, *26*(6), 1581–1595. https://doi.org/10.5194/angeo-26-1581-2008
Feldstein, I. I., Lyatskaya, A. M., Sumaruk, P. V., & Shevnina, N. F. (1975). Ionization of the F-layer of the ionosphere and variations of the magnetic field in the near-polar region. *Geomagnetism and Aeronomy*, *15*, 1021–1027.
Friis-Christensen, E., Lühr, H., Knudsen, D., & Haagmans, R. (2008). Swarm—An Earth observation mission investigating Geospace. *Advances in Space Research*, *41*(1), 210–216. https://doi.org/10.1016/j.asr.2006.10.008
Haaland, S., Lybekk, B., Maes, L., Laundal, K., Pedersen, A., Tenfjord, P., et al. (2017). North-south asymmetries in cold plasma density in the magnetotail lobes: Cluster observations. *Journal of Geophysical Research: Space Physics*, *122*, 136–149. https://doi.org/10.1002/2016JA023404
Haaland, S., Svenes, K., Lybekk, B., & Pedersen, A. (2012). A survey of the polar cap density based on Cluster EFW probe measurements: Solar wind and solar irradiation dependence. *Journal of Geophysical Research*, *117*, A01216. https://doi.org/10.1029/2011JA017250
Hatch, S. M., Haaland, S., Laundal, K. M., Moretto, T., Yau, A. W., Bjoland, L., et al. (2020). CHAMP and swarm solar activity- and height-scaled polar cap plasma density measurements (version v0) [data set, zenodo]. https://doi.org/10.5281/zenodo.3813145
Holland, P. W., & Welsch, R. E. (1977). Robust regression using iteratively reweighted least-squares. *Communications in Statistics - Theory and Methods*, *6*(9), 813–827. https://doi.org/10.1080/03610927708827533
Horwitz, J. L., Ho, C. W., Scarbro, H. D., Wilson, G. R., & Moore, T. E. (1994). Centrifugal acceleration of the polar wind. *Journal of Geophysical Research*, *99*(A8), 15,051–15,064. https://doi.org/10.1029/94JA00924
Hu, A., Carter, B., Currie, J., Norman, R., Wu, S., Wang, X., & Zhang, K. (2019). Modeling of topside ionospheric vertical scale height based on ionospheric radio occultation measurements. *Journal of Geophysical Research: Space Physics*, *124*, 4926–4942. https://doi.org/10.1029/2018JA026280
Huber, P. J. (1973). Robust regression: Asymptotics, conjectures and Monte Carlo. *The Annals of Statistics*, *1*(5), 799–821. https://doi.org/10.1214/aos/1176342503
Ivanov-Kholodnyy, G. S. (1962). Ionization of the upper atmosphere by solar short-wave radiation. *Geomagnetism and Aeronomy*, *2*, 561.
Khocholava, G. M. (1977). On diffusion-recombination parameters in the F-region of the ionosphere. *Journal of Atmospheric and Terrestrial Physics*, *39*, 389–391. https://doi.org/10.1016/S0021-9169(77)90154-4
Klumpar, D. M. (1979). Transversely accelerated ions: An ionospheric source of hot magnetospheric ions. *Journal of Geophysical Research*, *84*(A8), 4229–4237. https://doi.org/10.1029/JA084iA08p04229
Knudsen, D. J., Burchill, J. K., Buchert, S. C., Eriksson, A. I., Gill, R., Wahlund, J. E., et al. (2017). Thermal ion imagers and Langmuir probes in the Swarm electric field instruments. *Journal of Geophysical Research: Space Physics*, *122*, 2655–2673. https://doi.org/10.1002/2016JA022571
Laundal, K. M., Cnossen, I., Milan, S. E., Haaland, S. E., Coxon, J., Pedatella, N. M., et al. (2017). North-South asymmetries in Earth's magnetic field—Effects on high-latitude geospace. *Space Science Reviews*, *193*, 225–257.
Laundal, K. M., & Richmond, A. D. (2016). Magnetic coordinate systems. *Space Science Reviews*, *206*, 27–59. https://doi.org/10.1007/s11214-016-0275-y
Lei, J., Wang, W., Burns, A. G., Luan, X., & Dou, X. (2016). Can atomic oxygen production explain the ionospheric annual asymmetry? *Journal of Geophysical Research: Space Physics*, *121*, 7238–7244. https://doi.org/10.1002/2016JA022648
Li, K., Förster, M., Rong, Z., Haaland, S., Kronberg, E., Cui, J., et al. (2020). The polar wind modulated by the spatial inhomogeneity of the strength of the Earth's magnetic field. *Journal of Geophysical Research: Space Physics*, *125*, e2020JA027802. https://doi.org/10.1029/2020JA027802
Li, K., Haaland, S., Eriksson, A., André, M., Engwall, E., Wei, Y., et al. (2012). On the ionospheric source region of cold ion outflow. *Geophysical Research Letters*, *39*, L18102. https://doi.org/10.1029/2012GL053297
Liu, L., & Chen, Y. (2009). Statistical analysis of solar activity variations of total electron content derived at Jet Propulsion Laboratory from GPS observations. *Journal of Geophysical Research*, *114*, A10311. https://doi.org/10.1029/2009JA014533
Liu, C., Perez, J. D., Moore, T. E., & Chappell, C. R. (1994). Low energy particle signature of substorm dipolarization. *Geophysical Research Letters*, *21*(3), 229–232. https://doi.org/10.1029/93GL02839
Lomidze, L., Knudsen, D. J., Burchill, J., Kouznetsov, A., & Buchert, S. C. (2018). Calibration and validation of Swarm plasma densities and electron temperatures using ground-based radars and satellite radio occultation measurements. *Radio Science*, *53*, 15–36. https://doi.org/10.1002/2017RS006415
Maes, L., Maggiolo, R., & De Keyser, J. (2016). Seasonal variations and north-south asymmetries in polar wind outflow due to solar illumination. *Annales Geophysicae*, *34*, 961–974. https://doi.org/10.5194/angeo-34-961-2016
McNamara, L. F., Cooke, D. L., Valladares, C. E., & Reinisch, B. W. (2007). Comparison of CHAMP and digisonde plasma frequencies at Jicamarca, Peru. *Radio Science*, *42*, RS2005. https://doi.org/10.1029/2006RS003491
Mendillo, M., Huang, C.-L., Pi, X., Rishbeth, H., & Meier, R. (2005). The global ionospheric asymmetry in total electron content. *Journal of Atmospheric and Solar-Terrestrial Physics*, *67*(15), 1377–1387. https://doi.org/10.1016/j.jastp.2005.06.021
Mikhailov, A. V., & Schlegel, K. (2001). Equinoctial transitions in the ionosphere and thermosphere. *Annales Geophysicae*, *19*, 783–796. https://doi.org/10.5194/angeo-19-783-2001
Milan, S. E. (2009). Both solar wind-magnetosphere coupling and ring current intensity control of the size of the auroral oval. *Geophysical Research Letters*, *36*, L18101. https://doi.org/10.1029/2009GL039997
Milan, S. E., Boakes, P. D., & Hubert, B. (2008). Response of the expanding/contracting polar cap to weak and strong solar wind driving: Implications for substorm onset. *Journal of Geophysical Research*, *113*, A09215. https://doi.org/10.1029/2008JA013340
Nilsson, H., Engwall, E., Eriksson, A., Puhl-Quinn, P. A., & Arvelius, S. (2010). Centrifugal acceleration in the magnetotail lobes. *Annales Geophysicae*, *28*, 569–576. https://doi.org/10.5194/angeo-28-569-2010

Nilsson, H., Waara, M., Marghitu, O., Yamauchi, M., Lundin, R., Rème, H., et al. (2008). An assessment of the role of the centrifugal acceleration mechanism in high altitude polar cap oxygen ion outflow. *Annales Geophysicae*, *26*, 145–157. https://doi.org/10.5194/angeo-26-145-2008

Nishida, A. (1966). Formation of plasmapause, or magnetospheric plasma knee, by the combined action of magnetospheric convection and plasma escape from the tail. *Journal of Geophysical Research*, *71*(23), 5669–5679. https://doi.org/10.1029/JZ071i023p05669

Pedregosa, F., Varoquaux, G., Gramfort, A., Michel, V., Thirion, B., Grisel, O., et al. (2011). Scikit-learn: Machine learning in Python. *Journal of Machine Learning Research*, *12*, 2825–2830.

Quinn, T. P., & Nisbet, J. S. (1965). Recombination and transport in the nighttime F layer of the ionosphere. *Journal of Geophysical Research*, *70*(1), 113–130. https://doi.org/10.1029/JZ070i001p00113

Rees, M. H. (1963). Auroral ionization and excitation by incident energetic electrons. *Planetary and Space Science*, *11*(10), 1209–1218. https://doi.org/10.1016/0032-0633(63)90252-6

Rees, M. H. (1982). On the interaction of auroral protons with the Earth's atmosphere. *Planetary and Space Science*, *30*(5), 463–472. https://doi.org/10.1016/0032-0633(82)90056-3

Rees, M. H. (1989). *Physics and chemistry of the upper atmosphere*. Cambridge, United Kingdom: Cambridge University Press.

Reigber, C., Lühr, H., Grunwaldt, L., Förste, C., König, R., Massmann, H., & Falck, C. (2006). CHAMP mission 5 years in orbit, *Observation of the Earth system from space* (pp. 3–15). Berlin/Heidelberg: Springer-Verlag. https://doi.org/10.1007/3-540-29522-4_1

Rhodes, B. (2019). Skyfield: High precision research-grade positions for planets and Earth satellites generator.

Richmond, A. D. (1995). Ionospheric electrodynamics using magnetic apex coordinates. *Journal of Geomagnetism and Geoelectricity*, *47*(2), 191–212. https://doi.org/10.5636/jgg.47.191

Rishbeth, H. (1962). Atmospheric composition and the F layer of the ionosphere. *Planetary and Space Science*, *9*(4), 149–152. https://doi.org/10.1016/0032-0633(62)90002-8

Rishbeth, H. (1997). The ionospheric E-layer and F-layer dynamos—A tutorial review. *Journal of Atmospheric and Solar-Terrestrial Physics*, *59*, 1873–1880. https://doi.org/10.1016/S1364-6826(97)00005-9

Rishbeth, H., & Müller-Wodarg, I. C. F. (2006). Why is there more ionosphere in January than in July? The annual asymmetry in the F2-layer. *Annales Geophysicae*, *24*(12), 3293–3311. https://doi.org/10.5194/angeo-24-3293-2006

Rother, M., Choi, S., Mai, W., Lühr, H., & Cooke, D. (2005). Status of the CHAMP ME data processing, *Earth observation with CHAMP results from three years in orbit* (pp. 413). https://doi.org/10.1007/3-540-26800-6_66

Sai Gowtam, V., & Tulasi Ram, S. (2017). Ionospheric annual anomaly—New insights to the physical mechanisms. *Journal of Geophysical Research: Space Physics*, *122*, 8816–8830. https://doi.org/10.1002/2017JA024170

Schunk, R., & Nagy, A. (2009). *Ionospheres* (Second). Cambridge: Cambridge University Press. https://doi.org/10.1017/CBO9780511635342

Shim, J. S., Kuznetsova, M., Rastätter, L., Hesse, M., Bilitza, D., Butala, M., et al. (2011). CEDAR electrodynamics thermosphere ionosphere (ETI) challenge for systematic assessment of ionosphere/thermosphere models: NmF2, hmF2, and vertical drift using ground-based observations. *Space Weather*, *9*, S12003. https://doi.org/10.1029/2011SW000727

Sotirelis, T., Newell, P. T., & Meng, C.-I. (1998). Shape of the open-closed boundary of the polar cap as determined from observations of precipitating particles by up to four DMSP satellites. *Journal of Geophysical Research*, *103*, 399–406. https://doi.org/10.1029/97JA02437

Stankov, S. M., & Jakowski, N. (2006). Topside ionospheric scale height analysis and modelling based on radio occultation measurements. *Journal of Atmospheric and Solar-Terrestrial Physics*, *68*(2), 134–162. https://doi.org/10.1016/j.jastp.2005.10.003

Thébault, E., Finlay, C. C., Beggan, C. D., Alken, P., Aubert, J., Barrois, O., et al. (2015). International geomagnetic reference field: The 12th generation. *Earth, Planets and Space*, *67*(1), 79. https://doi.org/10.1186/s40623-015-0228-9

Torr, D. G., Torr, M. R., & Richards, P. G. (1980). Causes of the F region winter anomaly. *Geophysical Research Letters*, *7*(5), 301–304. https://doi.org/10.1029/GL007i005p00301

van der Meeren, C., Burrell, A. G., & Laundal, K. M. (2018). apexpy: ApexPy version 1.0.3.

Velinov, P. (1970). Solar cosmic ray ionization in the low ionosphere. *Journal of Atmospheric and Terrestrial Physics*, *32*, 139–147. https://doi.org/10.1016/0021-9169(70)90187-X

Virtanen, P., Gommers, R., Oliphant, T. E., Haberland, M., Reddy, T., Cournapeau, D., et al. (2020). SciPy 1.0: Fundamental algorithms for scientific computing in python. *Nature Methods*, *17*, 261–272. https://doi.org/10.1038/s41592-019-0686-2

Xiong, C., Stolle, C., & Park, J. (2018). Climatology of GPS signal loss observed by Swarm satellites. *Annales Geophysicae*, *36*(2), 679–693. https://doi.org/10.5194/angeo-36-679-2018